Unusual Quantum Interference in the S−1 State of DABCO and Observation of Intramolecular Vibrational Redistribution

7 AUTHORS, INCLUDING:

Lionel Poisson

French National Centre for Scientific Resea…

106 PUBLICATIONS **929** CITATIONS

SEE PROFILE

David H Parker

Radboud University Nijmegen

204 PUBLICATIONS **4,808** CITATIONS

SEE PROFILE

Mama Nsangou

University of Maroua

41 PUBLICATIONS **244** CITATIONS

SEE PROFILE

Majdi Hochlaf

Université Paris-Est Marne-la-Vallée

240 PUBLICATIONS **1,592** CITATIONS

SEE PROFILE

Unusual Quantum Interference in the S$_1$ State of DABCO and Observation of Intramolecular Vibrational Redistribution[†]

Lionel Poisson,*,‡ Raman Maksimenska,$^{‡,#}$ Benoît Soep,‡ Jean-Michel Mestdagh,‡ David H. Parker,§ Mama Nsangou,$^{∥}$ and Majdi Hochlaf*$^{,⊥}$

Laboratoire Francis Perrin, CNRS URA 2453, CEA, IRAMIS, Service des Photons Atomes et Molécules, F-91191 Gif/Yvette, France, Department of Molecular and Laser Physics, Institute for Molecules and Materials, Radboud University Nijmegen, Heyendaalseweg 135, 6525 ED Nijmegen, The Netherlands, Department of Physics, Faculty of Sciences, University of Ngaoundere, P.O. Box 454 Ngaoundere, Cameroon, and Laboratoire Modélisation et Simulation Multi-Echelle, Université Paris-Est, MSME FRE 3160 CNRS 5 bd Descartes, 77454 Marne-la-Vallée, France

In this paper we report an experimental study of the time-resolved response of the molecule 1,4-diazabicyclo[2.2.2]octane (DABCO) to 266.3 nm electronic excitation of the S$_1$ state with a femtosecond laser. Rotational decoherence and vibrational oscillation within the S$_1$ state are observed. We performed state-of-the-art ab initio calculations on the ground and low electronic states of the neutral molecule and the cation, which assist in the assignment of the observed photoelectron signals. Using our theoretical and spectroscopic data, the experimental findings are interpreted in terms of an unusual quantum interference between two different vibrational modes, with only the $\nu = 1$ level of each mode being populated.

Introduction

The properties of triethylenediamine (1,4-diazabicyclo-[2,2,2]octane, DABCO; see Figure 1) have been intensively investigated in the past because of its peculiar structure, which makes it a model molecule for spectroscopy (electronic[1−3] and vibrational[4−6]) and theoretical investigations.[7] Indeed, DABCO has simultaneously a strong rigidity, a high symmetry (D_{3h}), and a well-defined interaction possibility between two equivalent lone pairs of electrons.[8] The D_{3h} symmetry character of the molecule induces some symmetry rules that especially forbid the S$_1$ ← S$_0$ one-photon transition.[5] Nevertheless, the molecule has unitary quantum yield for fluorescence.[2] Thus, no conical intersection is predicted with the ground state, and no dynamics are expected on S$_1$ except for intramolecular vibrational redistribution (IVR). In terms of relaxation dynamics, the interest of this molecule has been therefore focused on the S$_2$ state.[9] However, diffraction experiments have shown that the shape of the potential energy surface along the torsion coordinate of the molecules is flat over a large range of torsion angles.[10] The torsional levels of DABCO are of low frequency (58 cm^{-1}, ref 6) and can be easily thermally populated. This population is associated with symmetry breaking, thereby allowing some one-photon processes for the excitation of the S$_1$ state. Excitation is especially efficient for the interaction with a broad spectral bandwidth of a femtosecond laser, which can excite a large number of vibrational levels available. The use of time-resolved photoelectron spectroscopy[11,12] becomes also a useful method to follow the IVR of this molecule excited to the first excited
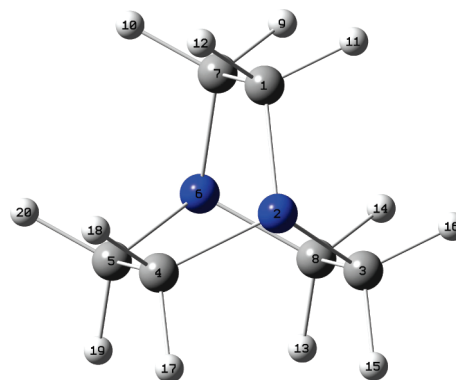

Figure 1. DABCO geometry.

state.[13] This work is also a contribution to the study of time-resolved IVR that was initiated by the group of Zewail[14] in 1984.

Experimental Section

Experimental Setup. The experimental setup is described in a previous paper[15] (see Figure 2). In the present case, the vapor pressure of DABCO at room temperature is high enough to make its direct injection in the main chamber, without using a heater, much more convenient than its introduction in a molecular beam. An experiment was performed in a supersonic expansion in He, but the photoelectron signal of cooled DABCO obtained is expected to be mixed with background DABCO. No significant difference was noted in the photoelectron spectra. Subsequently, the present results are obtained with DABCO as a background gas in the main chamber.

In brief, the molecule of interest is probed by a femtosecond laser (LUCA part of the SLIC European facility). The fundamental laser wavelength was measured to be 792 nm with a full width at half-maximum (fwhm) of 22 nm. Second and third harmonics were generated by doubling and mixing in BBO

Figure 2. Experimental setup.

Figure 3. Photoelectron spectrum [1+1] at 266.3 nm. Dashed lines represent the fit functions used to calculate β_2 and β_4 for each part of the spectrum.
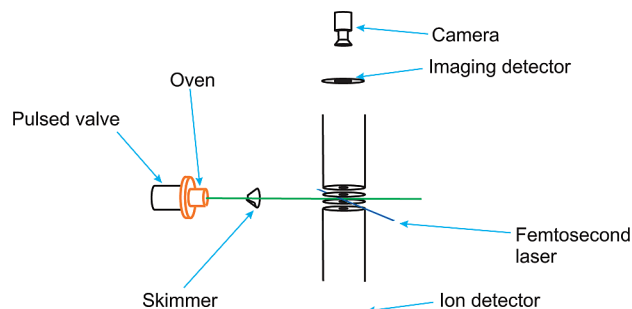
crystals.[16] The harmonics were measured to be respectively 399.2 nm (fwhm 5 nm) and 266.3 nm (fwhm 2.1 nm). Ions and electrons are extracted orthogonally to the molecular beam, where the ions can be detected by a time-of-flight spectrometer. Velocity distributions of both the ions and electrons can be monitored by a VMI[17] device. Low energy ions and electrons are especially well-resolved by this technique. However, since information is extracted from an angular distribution spread over a surface, a greater number of averages must be recorded to achieve equivalent signal-to-noise ratios as obtained by ordinary mass spectrometry. This drawback is partially compensated by the 4π steradian collection of the charged particles.

The energy profile and ejection angles of the ions or electron detected can be reconstructed from the raw data by a pBASEX algorithm[18,19] based on the inverse Abel transform. This fit algorithm provides the contribution to the raw image of each level requested of the Legendre polynomial functions, Pn, as a function of the radius.

Energy calibration was performed by irradiation of O_2 molecules by the third harmonic of the laser, which shows a vibrational progression corresponding to the $X^2\Pi_g \leftarrow X^3\Sigma_g^-$ transition (IE = 12.0697 eV); this can be assigned and accurately fitted.[16] The calibration used in the present paper is E (eV) = $(8.6 \pm 0.3) \times r^2 \times 10^{-5}$, where r is the distance from the center of the image. The apparatus function is estimated about $\Delta E/E$ = 7%.

Experimental Results. The results section is organized as follows. First, the two photon photoelectron spectra are recorded to point out the ionization process. Then, two-color time-resolved experiments are carried out with the 266.3 pump and either 399.2 nm or 2 × 792 nm ionization, where the evolution
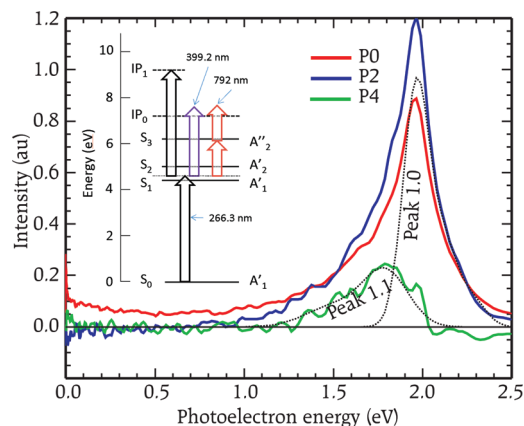
of each energy component can be followed in the photoelectron spectrum. The theoretical section describes the orbital structures and energies of excited states of DABCO and its cation DABCO$^+$.

Single color ionization of the free molecule by the third harmonic of the laser (266.3 nm) is induced by a two photon process and shows an electron energy peaking at 1.96 ± 0.1 eV (see energy level diagram and electron kinetic energy (KE) distribution, Figure 3). The photoelectron spectra (PE) reveals a broad band about 0.8 eV wide, from about 1.3 to 2.2 eV. The β_2 = P2/P0 and β_4 = P4/P0 anisotropy factors are obviously not constant through this spectrum. A set of two functions was defined to fit the photoelectron spectrum for each Legendre polynomial contribution (see functions in Figure 3). The characteristics of these bands are represented in Table 1. The vertical ionization energy (IE) of DABCO is described to be at 7.32 eV and the adiabatic one at 7.19 eV.[20] The corresponding electron KE, using the third harmonic of the laser, is expected to be also respectively 2.00 and 2.13 eV. The energy of the first electronic excited state of the DABCO$^+$ is estimated to be at 2.03 eV above the IE (see Table 4) and its formation should induce the formation of close to zero energy electrons. The shape of the spectrum will be discussed later.

Two-color studies were also carried out where the third harmonics of the laser was used to excite the free molecule.

TABLE 1: Parameters of the Photoelectron Spectrum Arising from Electronic Band That Composes the [2+0] 266.3 nm, [1+2′] 266.3−792 nm, and [1+1′] 266.3−399.2 nm Ionization of DABCO (Figure 3)

	[2+0] 266.3 nm		[1+2′] 266.3 nm/792 nm	
	peak 1.0	peak 1.1	peak 2.0	peak 2.1
peak energy	1.96 ± 0.07 eV	1.78 ± 0.06 eV	424 ± 15 meV	620 ± 22 meV
fwhm	210 ± 10 meV	400 ± 50 meV	29 ± 4 meV	53 ± 5 meV
$\beta_2^{\parallel}$	1.37 ± 0.1	1.47 ± 0.1	2.06 ± 0.1	1.8 ± 0.1
$\beta_4^{\parallel}$	0.02 ± 0.1	0.65 ± 0.1	0.5 ± 0.2	−0.2 ± 0.5
$\beta_2^{\perp}$	not applicable	not applicable	1.8 ± 0.2	0.83 ± 0.1
$\beta_4^{\perp}$	not applicable	not applicable	0.1 ± 0.1	−1.1 ± 0.3

	[1 + 2′] 266.3 nm/probe			
	peak 3.0		peak 3.1	
peak energy	376 ± 20 meV		477 ± 30 meV	
fwhm	37 ± 5 meV		42 ± 5 meV	
probe wavelength	792 nm	399.2 nm	792 nm	399.2 nm
$\beta_2^{\parallel}$	2.2 ± 0.1	0.80 ± 0.1	1.9 ± 0.2	not applicable
$\beta_4^{\parallel}$	1.1 ± 0.2	0.08 ± 0.2	−0.3 ± 0.5	not applicable
$\beta_2^{\perp}$	1.8 ± 0.1	0.89 ± 0.1	1.3 ± 0.2	not applicable
$\beta_4^{\perp}$	0.8 ± 0.2	0.17 ± 0.2	−0.15 ± 0.3	not applicable

Quantum Interference in the S₁ State of DABCO

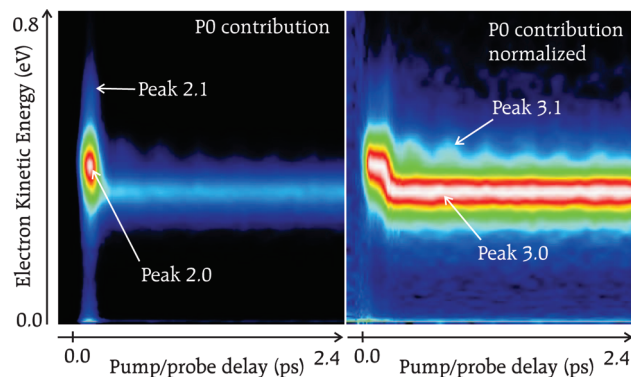*J. Phys. Chem. A, Vol. 114, No. 9, 2010* **3315**

Figure 4. Time-resolved photoelectron spectrum for DABCO in the gas phase, pumped by 266.3 nm and probed by 792 nm. Both laser polarizations are parallel to the detector. Only the P0 (zero-order of the Legendre polynomial decomposition) is represented.
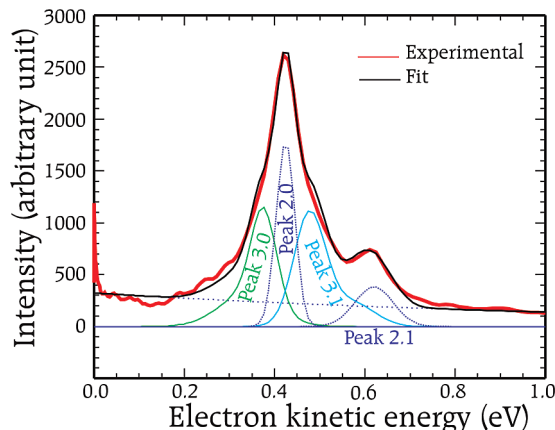

Figure 5. Fit of the photoelectron spectrum by the functions used for the data treatment of Figure 4. The experimental data are the photoelectron spectrum collected near the cross correlation of the lasers (see Figure 4).
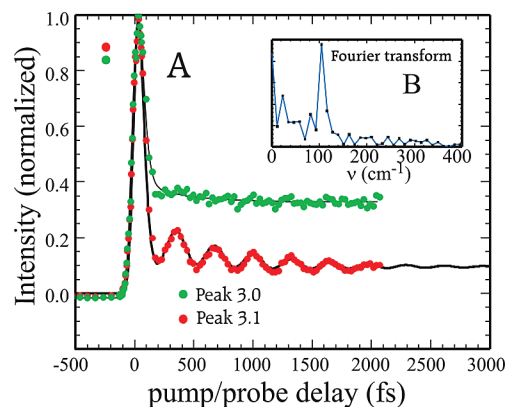

Figure 6. Fit of Figure 4 by the functions plotted in Figure 5. (A) Time evolution for two photoelectron bands, superimposed with the corresponding fit described in the text. Both fit curves are convoluted with a 60 fs fwhm Gaussian. (B) Fast Fourier transform of the experimental data starting at 500 fs.

Inspecting the (one-photon) absorption spectra of refs 1 and 5 indicates that the laser excites the higher vibrational levels of S₁ state. Several vibrational levels should be populated within the 310 cm⁻¹ bandwidth of the laser that covers the range 0_0^0 +[1610−1920 cm⁻¹]. Reference 21 shows the DABCO absorption spectrum for the corresponding laser energy range.

The excited molecule is probed by ionization with the fundamental (792 nm) or the second harmonic (399.2 nm) of the laser (see energy diagram of Figure 3). Figure 4 displays the photoelectron spectrum versus the time delay between the pump (266.3 nm) and the probe (792 nm). Two resonances appear within the laser autocorrelation (424 ± 15 meV, peak 2.0 in Table 1 and 620 ± 22 meV, peak 2.1 in Table 1). Peak 2.1 is weak but clearly visible when displaying Figure 4 at a higher sensitivity scale. At later delay times, the 434 mV peak shifts to a slightly lower energy (376 ± 20 meV, peak 3.0 in Table 1). At the same time an oscillation is visible at higher energies (477 ± 30 meV, peak 3.1 in Table 1); see Figure 4.

A 90° rotation of the pump polarization induces a reduction in the relative intensity observed between the signal detected at the cross-correlation time and the one at longer times.

The use of the 399.2 nm wavelength as the probe reveals solely the 3.0 band (see Figure 7). Therefore, all other bands come from intermediate resonances in the multiphoton ionization process. The oscillation that was clearly identified with the 792 nm probe is also no longer observed with the second harmonic as the probe.

The two photon ionization of the initially populated S₁ state may be enhanced by an ionization resonance with the S₃ molecular state peaking[1] at about 50200 ± 150 cm⁻¹ while [266.3 + 792] nm ≈ 50150 cm⁻¹.

To extract the time evolution parameters from the experimental data of Figure 4, first the photoelectron signal is fitted for each delay time by a sum of several functions as plotted in Figure 5. The "background" function is also adjusted to fit the low energy part of the experimental data. The two main functions are chosen to fit as well as possible the experimental data. Each is composed of the sum of two Gaussian functions.

The laser cross correlation function is estimated experimentally to fit a 60 fs FWMH Gaussian function for this experiment. Hence, all the decays functions are convoluted by a such Gaussian function.

The time evolution of the two main fitting functions is plotted in Figure 6. The time evolution of the lowest energy one (376 ± 20 meV, peak 3.0) can be fitted by a two-step kinetic model involving three transients.[15] The time constants of the corre-

sponding two exponential decays are $\tau_1 = 30 \pm 10$ fs and $\tau_2 = 360 \pm 100$ fs. The use of the 400 nm as the probe shows only the second time component of this band after a rise time $\tau_1 = 30 \pm 10$ fs and a small energy shift in the first tens of femtosecond of the dynamics followed by the τ_2 time decay.

The time evolution of the highest energy component (477 ± 30 meV, peak 3.1) shows clear oscillations, as displayed in Figure 6. Figure 6B depicts the fast Fourier transform of the experimental data. The main oscillation period is $\tau_{osc} = 323 \pm 10$ fs. Fitting the signal by using this value leads to a phase shift from zero of $\phi_{osc} = 13 \pm 10$ fs, and the disappearance of the oscillations with two exponential decays of respectively $\tau_{\phi 1} = 45 \pm 10$ fs and $\tau_{\phi 2} = 850 \pm 100$ fs. The mean value of the signal decays with a $\tau_{o1} = 500 \pm 150$ fs time constant, which is probably linked to the τ_2 decay-time value. The decay of the oscillations where monitored up to 3.6 ps.

Theoretical Approaches and Results

Theoretical Method. State-of-the-art ab initio calculations on the ground and low electronic states of the neutral molecule and the cation were performed using the MOLPRO program suite.[22] The hydogen, nitrogen, and carbon atoms are described using the generally contracted cc-pVDZ, aug-cc-pVDZ, and aug cc-pVTZ basis sets of Dunning.[23] For the largest basis set, this results in 644 contracted Gaussian type orbitals (GTOs) that
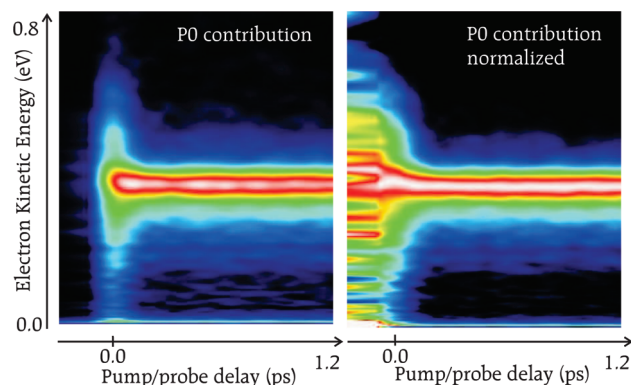
Figure 7. Time-resolved photoelectron spectrum of DABCO in the gas phase, pumped by 266.3 nm and probed by 399.2 nm. Both laser polarizations are parallel to the detector. Only the P0 (zero-order of the Legendre polynomial decomposition) is represented.

need to be considered. We performed the calculations in the C_{2v} point group when computing the potential curves. The geometry optimizations are done in the C_1 point group using the standard options implemented in MOLPRO.

For the DABCO and DABCO$^+$ electronic excited states calculations, we start with RHF calculations on the electronic ground state of the neutral molecule. Then, the electronic structure computations are done using the full valence complete active space self-consistent field (CASSCF) approach[24] followed by the internally contracted multireference configuration interaction (MRCI) technique.[25,26] Both of them are implemented in the MOLPRO program suite.[22] For a better accuracy we quote also the Davidson corrected energies (MRCI+Q).[27] For the neutral molecule, we considered the two lowest singlet and triplet electronic states computed at the equilibrium geometry of its ground state optimized at the MP2/cc-pVDZ (cf. Table 2 and Figure 1). For calculation of the cationic states, we treated two electronic states per C_{2v} symmetry of doublet and quartet spin-multiplicities. The ion is taken at the equilibrium geometry of its ground state derived from our MP2/cc-p-VDZ calculations. In CASSCF, all electronic states having the same spin multiplicity are averaged together with equal weights using the MOLPRO state averaging procedure. For the symmetry designation of electronic states, the C_3 axis of D_{3h} coincides with the *x*-axis.

In the C_{2v} point group, the molecular orbitals (MOs) of DABCO decompose as follows: $3a_1 + 3b_1 + 1b_2 + 1a_2$ core orbitals and $13a_1 + 13b_1 + 9b_2 + 9a_2$ valence orbitals, which results in 44 valence MOs to be considered in full valence CASSCF calculations. This is out of the range of the available MOLPRO version that treats only 16 active orbitals. Several tests were performed to reduce the size of the active space without disturbing strongly the pattern of the lowest electronic states of these molecular species. Our best compromise is when

the active space is constructed by the $(10 \text{ to } 13)a_1 + (8 \text{ to } 11)b_1 + (6 \text{ to } 7)b_2 + (5 \text{ to } 6)a_2$ MOs. The MOs located below in energy are kept doubly occupied and frozen during the CASSCF calculations. At the MRCI level of theory, all configurations with coefficients larger than 0.1 in the CI expansion of the CASSCF wave functions were taken as reference, and all electrons were correlated. This leads to about $(1-4) \times 10^8$ uncontracted configuration state functions (CSFs) for each symmetry of the C_{2v} point group to be treated.

Theoretical Results. We list in Table 2 the results for the calculations on neutral DABCO and the ionized DABCO$^+$ species. Similar to the neutral, the cation presents a D_{3h} symmetry. For the neutral, our structural parameters are consistent with previous works[28] and with experimental results.[10] At equilibrium, we calculate the following rotational constants for DABCO: $A_e = 2.65$ GHz and $B_e = C_e = 2.49$ GHz. On ionization of DABCO, the CH, CN, and CC internuclear separations and the in-plane angles are slightly affected, whereas the NN distance is shortened (i.e., the cage is compressed). Therefore, we expect a relatively short vibrational progression in the photoelectron spectra of DABCO because of favorable Franck−Condon factors. At the CASSCF/MRCI+Q/aug-cc-pVTZ level of theory, we compute a vertical ionization energy (VIE) of 7.31 eV, which is consistent with the experimental VIE of 7.3013 eV deduced from high resolution ZEKE spectra of Watkins et al.[20]

Table 3 lists the CASSCF, MRCI, and MRCI+Q vertical excitation energies of the DABCO electronic states of interest and using three different basis sets: cc-pVDZ, aug-cc-pVDZ, and aug-cc-pVTZ. These energies are given with respect to the DABCO ground state. This table gives also their dominant electron configurations quoted at DABCO equilibrium geometry. These electronic states present a monoconfigurational character and they can be described by a unique configuration (weights larger than 90%). They are associated with an excitation of an electron from the $6a'_1$ MO into the vacant $(7a'_1)$, $(5e'')$, $(6a''_2)$, and $(6e')$ MOs.

Using the smallest basis set, we compute the S_1-S_0 transition at 6.34 eV, independently from the electron correlation level. This value is definitely larger than the experimentally established value for this transition in DABCO, 4.4365 ± 0.0003 eV obtained by Consalvo et al.[4] by a laser induced fluorescence experiment. The inclusion of diffuse atomic orbitals (either in aug-cc-pVDZ or in aug-cc-pVTZ) reduced this transition energy to about 4.1−4.7 eV, i.e., in close accord with the experimental value. This is a signature of the valence-Rydberg nature of the excited electronic states of DABCO. Close examination of the wave functions of these electronic states shows that they possess about 90% 3s and 4s Rydberg character and only 10% valence character. The upper singlets and triplets are lying close in energy to S_1 and to T_1 (cf. Table 3 for more details). This may

TABLE 2: Structure for DABCO and DABCO$^+$ Calculated at the MP2/cc-pVDZ and MP2/aug-cc-pVDZ Levels of Theory

	DABCO			DABCO$^+$	
	MP2/cc-pVDZ	MP2/aug-cc-pVDZ	exp[a]	MP2/cc-pVDZ	MP2/aug-cc-pVDZ
angle C−N−C, deg	108.4	108.4	108.7 ± 0.4	111.8	111.9
angle N−C−C, deg	110.5	110.5	110.2 ± 0.4	107.0	107.0
angle N−C−H, deg	107.9	107.7		110.2	110.2
distance C−H, Å	1.104	1.103	$1.11_0 \pm 0.01_2$	1.100	1.098
distance C−N, Å	1.472	1.477	1.472 ± 0.007	1.439	1.442
distance C−C, Å	1.561	1.564	1.562 ± 0.009	1.631	1.637
distance N−N, Å	2.594	2.599		2.474	2.478

[a] Reference 10.

Quantum Interference in the S$_1$ State of DABCO

J. Phys. Chem. A, Vol. 114, No. 9, 2010 **3317**

TABLE 3: Vertical Excited State Energies Calculated at Different Levels of Theory[a]

state	configuration() weight of the principal configuration	cc-pVDZ			Aug-cc-pVDZ			Aug-cc-pVTZ		
		CASSCF	MRCI	MRCI+Q	CASSCF	MRCI	MRCI+Q	CASSCF	MRCI	MRCI+Q
$\tilde{X}^1A_1'$	(0.99): ...(5e')^4(4e'')^4(5a$_2'$)^2(6a$_1'$)^2	0.00	0.00	0.00	0.00	0.00	0.00	0.00	0.00	0.00
$\tilde{a}^1A_1'$	(0.98): ...(5e')^4(4e'')^4(5a$_2'$)^2(6a$_1'$)^1(7a$_1'$)^1	6.34	6.61	6.38	4.66	4.18	4.76	4.10	4.60	4.78
$\tilde{a}^3A_1'$	(0.98): ...(5e')^4(4e'')^4(5a$_2'$)^2(6a$_1'$)^1(7a$_1'$)^1	6.52	6.16	6.07	4.62	4.59	4.72	4.52	4.69	4.82
$\tilde{b}^1E'$	(0.99): ...(5e')^4(4e'')^4(5a$_2'$)^2(6a$_1'$)^1(6e')^1	7.16	7.34	7.21	5.12	4.58	5.25	4.50	5.04	5.23
$\tilde{b}^3E'$	(0.99): ...(5e')^4(4e'')^4(5a$_2'$)^2(6a$_1'$)^1(6e')^1	7.37	7.09	7.04	5.09	5.00	5.23	4.94	5.16	5.31
$\tilde{c}^3A_2''$	(0.99): ...(5e')^4(4e'')^4(5a$_2'$)^2(6a$_1'$)^1(6a$_2'$)^1	8.14	8.03	7.90	5.32	5.34	5.41	5.13	5.30	5.39
$\tilde{c}^1E''$	(0.98): ...(5e')^4(4e'')^4(5a$_2'$)^2(6a$_1'$)^1(5e'')^1	8.64	8.93	8.84	5.81	5.24	5.97	5.12	5.69	5.89
$\tilde{d}^3E''$	(0.98): ...(5e')^4(4e'')^4(5a$_2'$)^2(6a$_1'$)^1(5e'')^1	8.92	8.80	8.68	5.79	5.67	5.95	5.57	5.83	5.99
$\tilde{d}^1A_2''$	(0.98): ...(5e')^4(4e'')^4(5a$_2'$)^2(6a$_1'$)^1(6a$_2'$)^1	9.06	11.1	10.6	5.86	5.31	6.00	6.34	6.78	6.82

[a] The ground state energy is taken as reference. Both singlet and triplet states are presented. Energies are in eV. The symmetry group is D_{3h}.

TABLE 4: Vertical Excited State Energies Calculated at Different Levels of Theory for the Geometry of the Ground State Ionic Molecule DABCO$^+$ [a]

state	configuration() weight of the principal configuration	Aug-cc-pVTZ		
		CASSCF	MRCI	MRCI+Q
$\tilde{X}^2A_1'$	(0.97): ...(5e')^4(4e'')^4(5a$_2'$)^2(6a$_1'$)^1	0.00	0.00	0.00
$\tilde{a}^2A_2'$	(0.97): ...(5e')^4(4e'')^4(5a$_2'$)^1(6a$_1'$)^2	1.93	2.01	2.03
$\tilde{b}^2E''$	(0.97): ...(5e')^4(4e'')^3(5a$_2'$)^2(6a$_1'$)^2	4.61	4.40	4.33
$\tilde{a}^4A_2'$	(0.99): ...(5e')^4(4e'')^4(5a$_2'$)^1(6a$_1'$)^1(7a$_1'$)^1	8.35	6.91	4.96
$\tilde{b}^4E''$	(0.99): ...(5e')^4(4e'')^4(5a$_2'$)^1(6a$_1'$)^1(6e')^1	9.18	7.71	5.76
$\tilde{c}^2E'$	(0.97): ...(5e')^3(4e'')^4(5a$_2'$)^2(6a$_1'$)^2	6.30	6.22	6.17
$\tilde{d}^2E'$	(0.85): ...(5e')^4(4e'')^4(5a$_2'$)^2(6e')^1	7.81	7.80	7.84
$\tilde{c}^4E'$	(0.99): ...(5e')^4(4e'')^4(5a$_2'$)^1(6a$_1'$)^1(6e')^1	9.13	7.92	8.47

[a] The ground state energy is taken as reference. Both doublet and quartet states are presented. Energies are in eV. Electron configurations are quoted at the D_{3h} equilibrium geometry of the neutral ground state.

favor the mixing of their wave functions by spin−orbit and vibronic couplings. However, the spin−orbit coupling integrals, evaluated in Cartesian coordinates over the CASSCF wave functions, between the singlet and the triplet electronic states of DABCO are found to be weak: Close to the equilibrium geometry of DABCO, they do not exceed 0.3 cm^{-1}. Therefore, we expect that spin−orbit conversion of singlet excited DABCO into triplet excited DABCO (and vice versa) are negligible on the time scale of these experiments.

Table 4 gives the dominant electron configuration and the vertical excitation energies of the lowest DABCO$^+$ doublets and quartets calculated using the CASSCF/aug-cc-pVTZ, CASSCF/ MRCI/aug-cc-pVTZ and CASSCF/MRCI+Q/aug-cc-pVTZ methodologies. These energies are calculated at equilibrium geometry of DABCO$^+$ (Table 2). The ground state of the cation, which we label D$_0$, is a doublet ($\tilde{X}^2$ A$_1'$) obtained after removal of an electron from the (6a$'_1$) MO. The other doublets (except the $\tilde{d}^2$E') are obtained after ejection of an electron from the outermost MOs of DABCO, whereas the $\tilde{d}^2$E' and the quartets are obtained after ejection of an electron from these orbitals with simultaneous excitation of another into a vacant molecular orbital.

We calculate the D$_1$−D$_0$ transition of the ion to be around 2 eV. Generally, the three multireference methods lead to similar results, except for the two lowest quartets (i.e., the $\tilde{a}^4$A$_2''$ and $\tilde{b}^4$E'' states) it is lowered from 8.35 eV at CASSCF, to 6.91 eV at MRCI, to 4.96 eV at MRCI+Q and to 9.18, 7.71 and 5.76 eV, respectively. Similar to the case for the neutral molecule, a high density of electronic states is noticeable, which favors their mutual interactions by nonadiabatic couplings. The DABCO photoelectron spectrum[29] appears to be compatible with a first excited state of the ion at around 2.0 eV above the IE.

Discussion

Franck−Condon (FC) Region. The single color photoelectron spectrum (Figure 3) suggests that two mechanisms participate in the in $\tilde{X}^1A_1' \rightarrow \tilde{X}^2A_1' + e^-$ ionization process. Peak 1.0 has a sharper profile (∼210 meV) than peak 1.1 (∼400 meV), which has in turn a stronger anisotropic component. In particular, only peak 1.1 shows up in the P4 anisotropy component. Accordingly, peak 1.1 is most likely induced by a nonresonant ionization mechanism since its anisotropy fits with the transition probability rule $\langle\psi_{DABCO}(\tilde{X}^1A_1')|\mu|\psi_{DABCO^+}(\tilde{X}^2A_1')\rangle \otimes \psi(e^-)\rangle \neq 0$. In contrast, peak 1.0, which has only a P2 component in its expansion should be induced by a resonant process going through an s-Rydberg state ($\tilde{a}^1A_1'$ fully symmetrical), losing the electronic polarization of the first transition ($\langle\psi_{DABCO}(\tilde{X}^1A_1')|\mu|\psi_{DABCO^*,\nu}(\tilde{a}^1A_1')\rangle\langle\psi_{DABCO^*,\nu}(\tilde{a}^1A_1')|\mu|\psi_{DABCO^+}(\tilde{X}^2A_1') \otimes \psi(e^-)\rangle \neq 0$). The two functions used for the fit (peak 1.0 and peak 1.1) are present also in the photoelectron spectrum induced by each process. The nonresonant process expands to a maximal energy given by the vertical IE (2.00 eV) since the resonant one is going up to the adiabatic IE (2.13 eV). The nonresonant process provides the FC projection of the vibrationless ground state wave function onto the ionic state without vibrational selection rules, since the resonant process shows the FC projection of the ground state to the S$_1$ state convoluted by the ionization to the ground state ion. The S$_1$ state is not purely Rydberg, some transitions involving the lowering of the vibrational excitation ($\Delta\nu = -1$) such as the D$_0$ ← S$_1$ 24$^0_1$ and D$_0$ ← S$_1$ 26$^0_1$ transitions, may occur, explaining the expansion in the electron kinetic energy to higher values.

Rotational Decoherence. Comparison of the band evolutions for the crossed and parallel polarizations (see Figure 8) reveals clearly that the τ_2 time corresponds to the randomization of the molecular orientation.[30] The rotational anisotropy function is defined as $r(\tau) = [I_\parallel(\tau) - I_\perp(\tau)]/[I_\parallel(\tau) + 2I_\perp(\tau)]$ is plotted in Figure 8. The minimum of the anisotropy functions is described as $\tau_{min} = (I/k_B T)^{1/2}$, where I is the moment of inertia of the molecule, T is the temperature, and k_B the Boltzmann constant. The maximum of the anisotropy functions peaks at 15%. As seen earlier in the results of calculations, the rotational constants of this symmetric-top molecule in its ground state geometry are $A_e = 2.65$ GHz, $B_e = C_e = 2.49$ GHz. At room temperature, this corresponds to a $\tau_r \sim 900$ fs. This value fits well with our results. Since the excited state is described to have a large 3s-Rydberg component, which has a pure spherical symmetry, such a behavior was not expected. Accordingly, the excited state contains some polarized valence component confirmed by the present calculations (∼10% mixing of valence-Rydberg). Note here that the detection of the anisotropy is possible only for an initially oriented population of DABCO. Actually, at first order
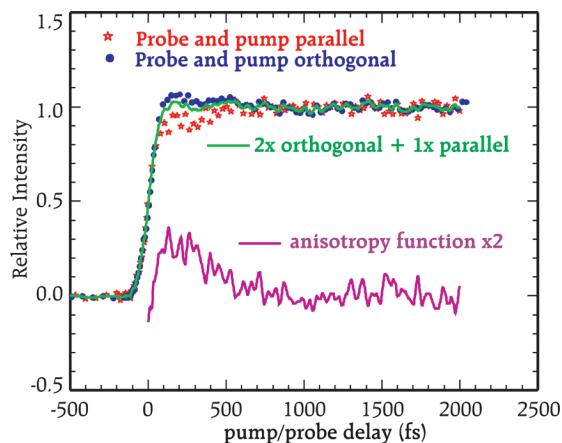
Figure 8. Time-resolved photoelectron spectrum for DABCO in the gas phase, pumped by 266.3 nm and probed by 399.2 nm. Comparison of crossed and parallel polarization. Only the P0 evolution of peak 3.0 is displayed. The spectra are normalized for long time delays.

the electronic transition, $\tilde{a}^1(A_1') \leftarrow \tilde{X}^1(A_1')$, does not provide such alignment. Quadripolar electric transition or vibronic coupling also participates in the excitation.[31] This would induce a transition along respectively either the $(x^2 + y^2)$ or z^2 (A_1') component, or (x, y) (E′) by dipolar momentum "borrowing" from, for example, the $\tilde{b}^1(E') \leftarrow \tilde{X}^1(A_1')$ transition (Herzberg–Teller vibronic coupling).[32]

Oscillation Period. The 100 cm^{-1} oscillation period observed in the pump probe experiment of free DABCO appears only with the two-photon ionization probe, indicating a resonance in the ionization process that filters the ionization of the initially excited wavepacket. The filter is typically a [1′+1′] resonance with a Rydberg state occurring only at a well-defined geometry. Let us consider the ionization probability as proportional to a product of the S_1-resonance overlap by the resonance-D_0 ion state overlap. As seen in the theoretical section, since S_1 has both valence and Rydberg character, it is not surprising that the potential energy surface is not parallel to the higher states. Moreover, the difference is expected to be stronger when far from the minimum of the S_1 state. According to the phase of the oscillations observed ($\phi_{osc} = 13 \pm 10$ fs), the resonance geometry is close to the initial geometry of the ground state. The oscillation period observed indicates the time taken by the wavepacket to reach a revival at the ground state geometry. An electronic transition that is enhanced by a Rydberg state resonance implies the propensity rule of $\Delta\nu = 0$ in the Rydberg-ion transition, due to the orthogonality of the vibrational wave functions,[33] since the ion and the intermediate Rydberg states have very close vibrational structure.

Several different interpretations could be invoked to understand these results. The multiphoton absorption spectrum reported by Parker et al.[5] shows that the excitation of the probe can populate coherently a series of vibrational bands. Indeed, in the excitation range estimated around 37350−37700 cm^{-1}, several bands are expected:[21,34] 37572.106 cm^{-1} ($S_1 \leftarrow S_0$ 24_0^1 + 5_0^1) − 37676.690 cm^{-1} ($S_1 \leftarrow S_0$ $24_0^1 + 4_0^1$) − 37386.001 cm^{-1} ($S_1 \leftarrow S_0$ $26_0^1 + 5_0^1$) − 37490.858 cm^{-1} ($S_1 \leftarrow S_0$ $26_0^1 + 4_0^1$) − 37547.612 cm^{-1} ($S_1 \leftarrow S_0$ 4_0^2) − 37338.444 cm^{-1} ($S_1 \leftarrow S_0$ 5_0^2) plus hot bands associated with the ν_{13} and ν_{36} low frequency motions, will be excited.

For the interpretation we can invoke the scenarios:

(i) Two vibrational states, each in a different mode, with energy differing by 100 cm^{-1} may be excited coherently, hence inducing interference between these two states. The ν_4 (cage

squashing mode[4]) and ν_5 modes fit with this hypothesis. The resulting wavepacket is somehow unusual. The usual case is indeed a coherent excitation of several levels in the same vibrational mode. It corresponds to a wavepacket along a single coordinate that is describing the deformation mode. Here a single level in two different modes is coherently excited. The oscillation results, in this case, in the quantum interference between the two modes. The description of the wavepacket motion is also not as straightforward as in the usual case, since it is no longer representable as a movement along a single coordinate. This quantum interference results in an observable oscillation if at least one of the atoms of the molecular frame is involved in both vibrational modes and if the detection is sensitive to this atom motion.

(ii) A more complex wavepacket can be imagined with the beating of two usual subwavepacket on different vibration level. For example, here the coherent excitation of the levels ν_4 (4_0^2 and $4_0^1 + \nu_x$) and ν_5 (5_0^2 and $5_0^1 + \nu_x$) may induce the interference oscillations. Since the energies of the two vibrational coordinates differ by 100 cm^{-1}, the interference revival is expected to appear at the same frequency. In this scenario, the beating between the oscillation of the two wavepackets is observed.

(iii) The average torsion mode[4] $\nu_{13}(a_1'')$ spacing of the molecule is spectroscopically determined to be at ∼100 cm^{-1}. According to the REMPI spectroscopy, excitation of this mode exclusively looks unlikely. However, the population of combination bands with simultaneous excitation of torsion mode with other vibrational modes is plausible. Regular wavepacket oscillations can also be observed in this case.

A similar approach was proposed for the explanation of oscillations observed with the NO_2 molecule.[35]

Scenarios i and ii suggest that high frequency modes are excited coherently and the observation of a defined region of the molecular vibration space by a resonant enhanced ionization filters the location of the atoms at one point of the potential energy surface (PES) linked to the Franck−Condon region (see ref 36). Scenario iii suggests only an intramolecular dynamics process involving a low frequency mode reaching the resonance region only at one point of its evolution.

The spectrum observed in the group of Ito does not show any evidence for the population of 4_0^2 or 5_0^2 levels with one photon excitation, whereas it is observed with a two photon excitation.[21] Indeed, the excitation of the molecule is allowed thanks to a relaxation of the symmetry rules. Hence scenario ii is very unlikely since 4_0^2 and 5_0^2 cannot be excited in the present experiment.

Furthermore, scenario iii implies that the $\nu_{13}(a''_1)$ vibrational mode should be excited simultaneously with another e″ vibrational mode to allow the transition. Moreover, as stated in the Experimental Section, the experiments performed at room temperature and in the supersonic beam of DABCO show the same oscillations. Since this vibrational state is the lowest in energy of the ground state[6] (54 cm^{-1}), it is significantly populated at room temperature up to about the fourth quantum. An obvious difference would also be expected in the dynamics observed on the cold DABCO of the supersonic beam and the DABCO at room temperature. This seems to disfavor scenario iii.

Energetic Considerations. The energy difference between peak 3.0 and peak 3.1 is about 101 ± 36 meV. Converted into wavenumbers, this corresponds to a vibration of 815 ± 29 cm^{-1}. The intermediate resonance in the ionization process allows this absorption through a relative displacement of the S_1 state along

Quantum Interference in the S_1 State of DABCO

J. Phys. Chem. A, Vol. 114, No. 9, 2010 **3319**

this coordinate from the geometry of the intermediate Rydberg. As the signal from the nonresonant process or the one-photon ionization with 399.2 nm is lower in energy, the resonance implies a ν_1^0 transition to convert vibrational into electronic energy. Consideration of the energy favors also scenario i because it involves a vibrational level of a such energy[4] ($\nu_{26} = 823$ cm^{-1}).

Decay of the Oscillations. The three scenarios invoked above suppose an exploration of the S_1 PES where the initial energy, which is located in very few vibrational modes, is redistributed over the accessible states of the deformation modes. In usual oscillations, several vibration levels of the same mode are populated, and the decay of the oscillation is due to broadening of the wavepacket by the anharmonicity of the levels populated. Here the situation is very different since in scenario i, which is favored, only one level of two different modes are populated, excluding also the broadening of the wavepacket by anharmonic consideration.

The oscillation decay can be decomposed into two exponential decays; a short time constant $\tau_{\phi 1} = 45 \pm 10$ fs followed by a longer one $\tau_{\phi 2} = 850 \pm 100$ fs. The first time decay may be linked to an enhancement of resonance at the autocorrelation time. For the second one, inverted into wavenumbers, gives a 6.2 ± 0.7 cm^{-1} interaction width between the states involved in the oscillations and other vibrational states (intermolecular vibrational redistribution).

As a result scenario i seems a better candidate to account for the observed oscillations. This would correspond to the unusual situation of a quantum interference between two vibrational modes, revealed by an accidental resonance in the multiphoton probe process.

Conclusion

We have carried out time-resolved photoelectron spectroscopy of DABCO molecules populated in the S_1 state. Simultaneously, high level calculations were performed on the S_0 and S_1 states of the neutral and its D_0 ionic state.

Intramolecular relaxation was studied in the S_1 state as indicated by the observation of oscillations decaying with several time constants. The oscillations are interpreted in terms of a quantum interference between two vibrational modes, a single level of each being populated. This type of quantum interference may be commonplace in many polyatomic systems but has not been characterized yet. Further theoretical calculations are needed to fully understand the corresponding motion of the molecular framework. The decay of this oscillation regime is viewed to correspond to a reduction of the population in the beating modes, due to intramolecular vibrational energy redistribution (IVR), which transfers the vibrational energy to other modes.

References and Notes

(1) Halpern, A. M.; Roebber, J. L.; Weiss, K. *J. Chem. Phys.* **1968**, *49*, 1348–1357.

(2) Halpern, A. M.; Danziger, R. M. *Chem. Phys. Lett.* **1972**, *16*, 72–76.

(3) Parker, D. H.; Avouris, P. *Chem. Phys. Lett.* **1978**, *53*, 515–520.

(4) Consalvo, D.; Oomens, J.; Parker, D. H.; Reuss, *J. Chem. Phys.* **1992**, *163*, 223–239.

(5) Parker, D. H.; Avouris, P. *J. Chem. Phys.* **1979**, *71*, 1241–1246.

(6) Quesada, M. A.; Wang, Z. W.; Parker, D. H. *J. Phys. Chem.* **1986**, *90*, 219–222.

(7) Galasso, V. *Chem. Phys.* **1997**, *215*, 183–190.

(8) Shang, Q. Y.; Bernstein, E. R. *Chem. Rev.* **1994**, *94*, 2015–2025.

(9) Smith, M. A.; Hager, J. W.; Wallace, S. C. *J. Phys. Chem.* **1984**, *88*, 2250–2255.

(10) Yokozeki, A.; Kuchitsu, K. *Bull. Chem. Soc. Jpn.* **1971**, *44*, 72–77.

(11) Stolow, A.; Bragg, A. E.; Neumark, D. M. *Chem. Rev.* **2004**, *104*, 1719–1757.

(12) Suzuki, T. *Annu. Rev. Phys. Chem.* **2006**, *57*, 555–592.

(13) Reid, K. L. *Int. Rev. Phys. Chem.* **2008**, *27*, 607–628.

(14) Syage, J. A.; Felker, P. M.; Zewail, A. H. *J. Chem. Phys.* **1984**, *81*, 4706–4723.

(15) Poisson, L.; Raffael, K. D.; Soep, B.; Mestdagh, J. M.; Buntinx, G. *J. Am. Chem. Soc.* **2006**, *128*, 3169–3178.

(16) Baklanov, A. V.; Janssen, L. M. C.; Parker, D. H.; Poisson, L.; Soep, B.; Mestdagh, J.-M.; Gobert, O. *J. Chem. Phys.* **2008**, *129*, 214306–9.

(17) Eppink, A.; Parker, D. H. *Rev. Sci. Instrum.* **1997**, *68*, 3477–3484.

(18) Garcia, G. A.; Nahon, L.; Powis, I. *Rev. Sci. Instrum.* **2004**, *75*, 4989–4996.

(19) Poisson, L. LV_pBASEX, 2009.

(20) Watkins, M. J.; Cockett, M. C. R. *J. Chem. Phys.* **2000**, *113*, 10560–10571.

(21) Gonohe, N.; Yatsuda, N.; Mikami, N.; Ito, M. *Bull. Chem. Soc. Jpn.* **1982**, *55*, 2796–2802.

(22) Werner, H.-J. MOLPRO, version 2008.3, a package of ab initio programs, 2008; see http://www.molpro.net.

(23) Dunning, T. H. *J. Chem. Phys.* **1989**, *90*, 1007–1023.

(24) Knowles, P. J.; Werner, H.-J. *Chem. Phys. Lett.* **1985**, *115*, 259–267.

(25) Werner, H.-J.; Knowles, P. J. *J. Chem. Phys.* **1988**, *89*, 5803–5814.

(26) Knowles, P. J.; Werner, H.-J. *Chem. Phys. Lett.* **1988**, *145*, 514–522.

(27) Langhoff, S. R.; Davidson, E. R. *Int. J. Quantum Chem.* **1974**, *8*, 61–72.

(28) Balakrishnan, G.; Keszthelyi, T.; Wilbrandt, R.; Zwier, J. M.; Brouwer, A. M.; Buma, W. J. *J. Phys. Chem. A* **2000**, *104*, 1834–1841.

(29) Heilbronner, E.; Muszkat, K. A. *J. Am. Chem. Soc.* **1970**, *92*, 3818–3821.

(30) Raffael, K.; Blanchet, V.; Chatel, B.; Turri, G.; Girard, B.; Garcia, I. A.; Wilkinson, I.; Whitaker, B. J. *Chem. Phys. Lett.* **2008**, *460*, 59–63.

(31) Vandenhoek, G.; Consalvo, D.; Parker, D. H.; Reuss, J. *Z. Phys. D* **1993**, *27*, 73–78.

(32) Herzberg, G. Electronic Spectra and Electronic Structure of Polyatomic Molecules. In *Molecular spectra and molecular structure*; D. Van Norstrand Co., Inc.: Princeton, NJ, 1967; Vol. III, p 137.

(33) Suzuki, T.; Wang, L.; Tsubouchi, M. *J. Phys. Chem. A* **2004**, *108*, 5764–5769.

(34) Consalvo, D.; Drabbels, M.; Berden, G.; Meerts, W. L.; Parker, D. H.; Reuss, *J. Chem. Phys.* **1993**, *174*, 267–276.

(35) Sanrey, M.; Joyeux, M. *J. Chem. Phys.* **2007**, *126*, 074301-8.

(36) Herzberg, G. Infrared and Raman spectra of Polyatomic molecules. In *Molecular spectra and molecular structure*; Kreiger Publishing Co.: Malabar, FL, 1991; Vol. II, p 63.

JP909464T